Design and Optimization of 3D Printed ASA Substrate Based Antenna for Wi-Fi 6E

Manju, Kamal Gurgar, Manish Bijaraniya, Garima Saini, and Balwinder S. Dhaliwal

***Abstract*—This paper presents design, optimization, and fabrication of a wideband microstrip patch antenna utilizing a 3D-printed acrylonitrile styrene acrylate (ASA) substrate for Wi-Fi 6E frequency band. The dielectric properties of the ASA substrate are determined using the ring resonator method. The bandwidth enhancement is achieved by modifying the conventional rectangular patch into a staircase-shaped structure and employing a partial ground plane. To fine-tune the antenna's resonant frequency and bandwidth, a combination of curve fitting and particle swarm optimization (PSO) algorithm is utilized. The antenna comprises a patch with dimensions of 16.86 mm ×12.5 mm, situated on square substrate of size 27.5 mm × 27.5 mm. The antenna demonstrates a -10 dB impedance bandwidth ranging from 5.98 GHz to 8.62 GHz and a peak gain of 3.6 dBi at 6.525 GHz. Simulation and experimental results show good agreement, highlighting the potential of ASA as a viable substrate material for Wi-Fi 6E band antenna applications.**

***Index Terms*—3D-printed ASA substrate, PSO, Wideband antenna, Wi-Fi 6E.**

Original Research Paper
DOI: 10.53314/ELS2630094M

I. Introduction

THE escalating demand for higher data rates in modern wireless communication systems has fueled the need for broader communication channels to support bandwidth-intensive applications. The advent of Wi-Fi 6E, which extends into the 6 GHz band, introduces an additional 1200 MHz of spectrum, significantly enhancing network capacity and performance [1], [2]. This expansion underscores the critical need for antenna designs that are compact, efficient, and capable of operating across a wide bandwidth to fully exploit the potential of the 6 GHz band. Recent research has proposed various antenna configurations tailored for Wi-Fi 6E, addressing the challenges of size, performance, and broadband operation. In [1], a bow-tie antenna design was progressively modified from a symmetric to an asymmetric configuration, followed by the introduction of corner cuts near the feed to generate an additional resonance thereby broadening the upper operating band and enabling coverage of the 2.45 GHz WLAN band and the entire 5.15–7.125 GHz Wi-Fi 6E spectrum. A compact narrow-border laptop antenna reported in [2] utilized multiple resonant modes to achieve dual-band operation covering both WLAN and Wi-Fi 6E bands. The compact dual-band notched ultra-wideband (UWB) multiple-input multiple-output (MIMO) antenna presented in [3] employed complementary split ring resonators (CSRRs) and split ring resonators (SRRs) to achieve a wide impedance bandwidth while suppressing unwanted interference bands. A circularly polarized dielectric patch antenna proposed in [4] achieved a 48.3% impedance bandwidth by exciting multiple resonant modes and incorporating FR4 branches within an air cavity. A broadband dual-antenna pair for Wi-Fi 6/6E applications was presented in [5], where merging resonant modes in open-cavity antennas enabled continuous coverage of the 5 GHz and 6 GHz bands while maintaining isolation greater than 22.67 dB. Another approach reported in [6] enhanced bandwidth by optimizing the feed network to simultaneously excite the TM_{10} and anti-phase TM_{20} modes, with hybrid coupling further broadening the operating band. More recently, a defected ground structure (DGS)-based antenna was proposed in [7], in which a partially rectangular ground plane improved impedance matching and enabled broadband operation from 5.1 to 7.2 GHz.

Conventional antenna substrates such as FR4 [1], [2], [4], [7] and RT/Duroid [3] possess fixed dielectric constants and loss tangents, which significantly limit design flexibility [8]. Moreover, achieving wideband performance using these materials often requires complex antenna geometries or additional matching structures, increasing fabrication complexity [9]-[11]. In contrast, 3D-printed antenna substrates enable the tailoring of effective dielectric properties through controlled infill density, internal air cavities, and substrate thickness variation, thereby providing antenna designers with an additional degree of freedom for application-specific designs [12], [13]. The

Manuscript received 25 February 2026. Received in revised form 16 June 2026 and 22 July 2026. Accepted for publication on September 6th, 2026

Manju is with the Electronics & Communication Engineering Department, National Institute of Technical Teachers Training and Research, Chandigarh 160019, India. (e-mail: manju.ece25@nitttrchd.ac.in, ORCiD: 0009-0009-5393-3609).

K. Gurgar was with the Electronics & Communication Engineering Department, National Institute of Technical Teachers Training and Research, Chandigarh 160019, India. (e-mail: gurgar0507.kamal@gmail.com, ORCiD: 0009-0005-0058-0492).

M. Bijaraniya is with the Electronics & Communication Engineering Department, National Institute of Technical Teachers Training and Research, Chandigarh 160019, India. (e-mail: manish.ece25@nitttrchd.ac.in, ORCiD: 0009-0005-8180-7539).

G. Saini is with the Electronics & Communication Engineering Department, National Institute of Technical Teachers Training and Research, Chandigarh 160019, India. (e-mail: garima@nitttrchd.ac.in, ORCiD: 0000-0001-6525-5192).

B. S. Dhaliwal is with the Electronics & Communication Engineering Department, National Institute of Technical Teachers Training and Research, Chandigarh 160019, India. (e-mail: bsdhaliwal@ymail.com, ORCiD: 0000-0001-5092-017X).

popular polymers used as 3D-printed substrates for antennas include polylactic acid (PLA), acrylonitrile butadiene styrene (ABS), polyethylene terephthalate glycol (PETG), and acrylonitrile styrene acrylate (ASA) [14]-[17]. ASA was selected as the substrate because of its superior mechanical, chemical, and environmental properties, making it well suited for outdoor antenna applications. Compared with ABS, ASA exhibits enhanced UV stability, weather resistance, and greater resistance to heat, oxidation, and a wide range of chemicals [18], [19]. Its high toughness, dimensional stability, and strong interlayer adhesion achieved during 3D printing ensure structural integrity, impact resistance, and reliable fabrication [18], [20]. Owing to these advantages and its widespread use in the automotive, electronics, marine, and healthcare sectors [19], [20], ASA is a robust and reliable substrate material for 3D-printed antennas intended for outdoor environments. These characteristics make them particularly attractive for portable and embedded wireless devices, where weight and mechanical durability and design flexibility are critical.

To meet the wideband requirements of Wi-Fi 6E (5.925–7.125 GHz), bandwidth enhancement can be achieved through techniques such as patch and ground geometry modification [10], metamaterial loading [11], electromagnetic bandgap (EBG) structures [21], and stacked patch configurations [22]. Among these approaches, geometry modification offers simplicity in fabrication and facilitates compact and low-cost antenna realization, which aligns well with the capabilities of 3D printing. Furthermore, the associated design parameters can be efficiently optimized using curve fitting and particle swarm optimization (PSO) techniques to accurately control resonant frequency and bandwidth performance [23]-[25].

Based on these considerations, a 3D-printed ASA substrate-based wideband microstrip patch antenna (MPA) is designed, simulated, fabricated, and experimentally validated in this work for Wi-Fi 6E applications. The proposed antenna design is optimized using curve fitting and PSO algorithm to get the desired resonant frequency and bandwidth coverage. Ansys high frequency structure simulator (HFSS) software is used to simulate the proposed antenna, with the design centered at 6.525 GHz, corresponding to the mid-band frequency of the Wi-Fi 6E spectrum and the target resonant frequency. The fabrication and characterization of the substrate are discussed in Section II. The antenna design and parametric analysis are detailed in Section III, while Section IV focuses on the optimization of the antenna design. The simulated and measured results are analyzed and discussed in Section V, and the key conclusions drawn from this study are summarized in Section VI.

II. Substrate Fabrication And Characterization

The substrate was fabricated using a Creality Ender 3 Pro 3D printer, with printing parameters detailed in Table I. These printing parameters were selected to ensure uniform material deposition, strong interlayer bonding, and dimensional stability of the 3D-printed ASA substrate, which are critical for consistent dielectric behavior [12], [16], [18]. Controlled printing conditions help minimize warping and internal voids, thereby reducing dielectric inhomogeneity and RF losses [13], [22]. A fully dense substrate configuration was adopted to achieve stable and repeatable electromagnetic performance at microwave frequencies [8], [13], [22]. The chosen infill strategy provides predictable mechanical strength and supports reliable antenna fabrication using FFF [8], [12], [16].

TABLE I
Printing parameters for substrate fabrication

S. No.	Parameter	Value
1	Extruder temperature	245 °C
2	Bed temperature	95 °C
3	Printing speed	50 mm/s
4	Layer thickness	0.2mm
5	Infill density	100 %
6	Infill pattern	Lines

A ring resonator, illustrated in Fig. 1, was designed to characterize the dielectric properties of ASA, based on the approach reported in [26], with an assumed dielectric constant (ε_r) of 2.68. The microstrip feedline width is calculated using (1) [27].

$$w = \frac{7.48h}{e^{\left(z_0\frac{\sqrt{\varepsilon_r+1.41}}{87}\right)}} - 1.25t \quad (1)$$

where h and t denote the substrate height and copper trace thickness, respectively. For a characteristic impedance of 50 Ω, w is obtained as 3.69 mm, Using the equations in [16], [26], the mean ring radius (r_m) of 4.9 mm was calculated at resonant frequency, 6.525 GHz. The coupling gap (g = 2 mm) was kept high to provide loose coupling and reduce the impact of capacitive loading [28].

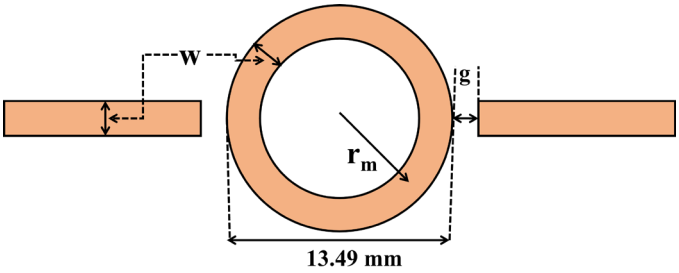


Fig. 1. Top layout of the ring resonator.

The vector network analyzer (VNA) was used to measure the transmission coefficient (S_{21}) of the fabricated ring resonator as shown in Fig. 2. The ring resonator exhibited periodic resonances in the S_{21} parameter, as illustrated in Fig. 3. The first resonant peak was observed at 6.56 GHz, with an associated insertion loss of -22.5 dB and a -3dB bandwidth of 380 MHz. These measurements, along with the ring design parameters, were used to calculate the dielectric constant and loss tangent (tan δ) using the equations provided in [16], [26]. For the fabricated ASA substrate, the dielectric constant and tan δ were found to be 2.72 and 0.0002, respectively.

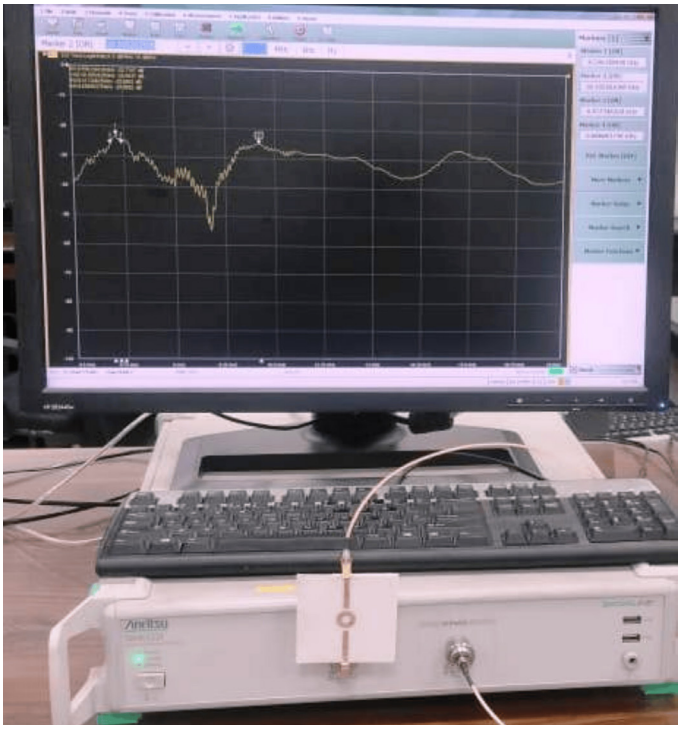


Fig. 2. S_{21} measurement using VNA.

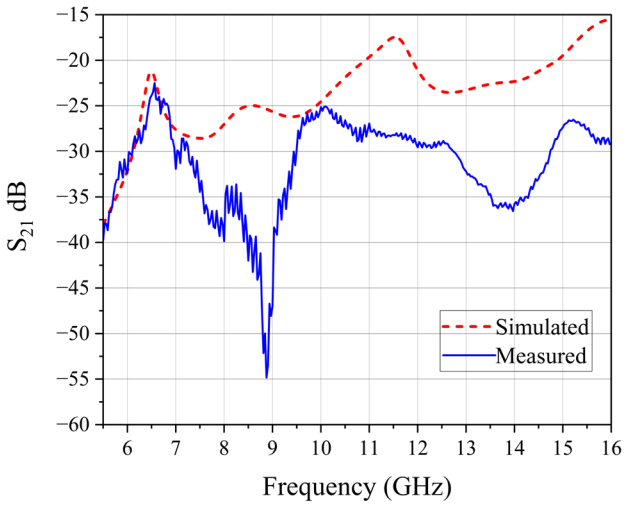


Fig. 3. Simulated and measured S_{21} plot of ring resonator.

III. Antenna Design

The initial antenna design considered in this work is a conventional rectangular microstrip patch antenna (MPA). In [17], the authors first investigated an initial rectangular MPA fabricated on a 3D-printed ASA substrate and operating at 6.525 GHz, with patch dimensions of width (W_p) 16.86 mm and length (L_p) 12.5 mm. This initial rectangular MPA exhibited a measured impedance bandwidth of only 200 MHz, indicating that a conventional rectangular MPA with these dimensions is insufficient to cover the entire Wi-Fi 6E frequency band (5.925–7.125 GHz), which requires an approximate fractional bandwidth of 18.4%. Therefore, bandwidth enhancement is essential to achieve full-band Wi-Fi 6E operation. To enhance the impedance bandwidth, the proposed antenna employs three design modifications: the introduction of slots in the radiating patch, optimization of the ground-plane length, and displacement of the patch from its central position along the substrate length. These modifications enable wideband operation while maintaining compact geometry and ease of fabrication. The proposed antenna retains the rectangular patch dimensions ($W_p \times L_p$) of the MPA in [17], but is realized on a square substrate with a side length of 27.5 mm. In contrast to the 32 mm × 27.5 mm substrate reported in [17], this reduction yields a more compact configuration.

The sequential design modifications are illustrated in Fig. 4. In step 1, To investigate the influence of ground plane length (L_G) on the resonant frequency and bandwidth, a parametric analysis was performed by varying L_G from 5.5 mm to 27.5 mm in steps of 1 mm. The results are presented in Fig. 5. It is observed that for, L_G = 5.5 mm the antenna achieves its maximum bandwidth of 2.18 GHz and resonates at 9.91 GHz. As L_G increases, the resonant frequency remains in this region above 9.5 GHz for values of L_G up to 16.5 mm, while the bandwidth gradually decreases. Beyond L_G = 17.5 mm, the resonant frequency shifts into the Wi-Fi 6E band; however, the bandwidth reduces sharply to approximately 200 MHz. Further for L_G values between 22.5 mm and 27.5 mm, the antenna resonates around 6.525 GHz with a bandwidth of approximately 200 MHz. These results highlight the trade-off between resonant frequency tuning and bandwidth.

For each subsequent design step (steps 2 to 4), the analysis was carried out in two stages. In the first stage, rectangular slots were introduced into the patch, and parametric analysis of their dimensions was performed using a full ground plane (L_G = 27.5 mm) to ensure that the antenna resonance remains within the desired Wi-Fi 6E band. In the second stage, the ground-plane length was systematically varied through parametric sweeps, using the finalized rectangular slot dimensions, to investigate its effect on the S_{11} response.

In step 2, two identical rectangular slots (RECT1) were etched at the patch corners adjacent to the microstrip feedline edge as shown in Fig. 4. The RECT1 slot dimensions were optimized through parametric analysis by varying both the length and width from 1 mm to 3 mm with a step size of 0.2 mm under a full ground-plane configuration. The corresponding results, presented in Fig. 6(a), shows that increasing the width of RECT1 from 1 mm to 3 mm, slightly degrades the impedance matching and shifts the resonant frequency to higher side by approximately 100 MHz, further, increasing the slot length shifts this variation on frequency scale slightly to higher side. The impedance bandwidth remains nearly constant at approximately 235 MHz throughout the parametric variation. The introduction of two rectangular slots in the patch in this step results in a slight improvement in performance, leading to an increase in bandwidth of approximately 35 MHz compared to step 1. After incorporating RECT1 slots in patch, further parametric analysis was conducted to examine the impact of ground plane length at this stage, which are shown in Fig. 6(b). For L_G < 15.5 mm,

the resonant frequency remains above 9.5 GHz. As L_G increases from 15.5 mm to 27.5 mm, the resonant frequency gradually shifts downward to 6.525 GHz.

In step 3, two additional identical rectangular slots (RECT2) were introduced adjacent to the RECT1 slots. The RECT2 dimensions were similarly optimized by sweeping the length and width from 1 mm to 2 mm with a step increment of 0.2 mm while maintaining a full ground plane. The parametric analysis of this is shown in Fig. 7(a). The effect of RECT2 dimensions on the resonant frequency is less significant compared to RECT1. In this analysis, the selected dimensions for RECT2 are 1.6 mm (width) and 1 mm (length), which provides the highest bandwidth of 287 MHz within parametric variation. After introducing RECT2, in patch the effect of ground plane length was examined, and the results are shown in Fig. 7(b). For, L_G = 5.5 mm, the antenna resonates at 10.58 GHz with a bandwidth of 2.97 GHz, and this resonance persists as L_G increases up to 16.5 mm. Beyond L_G = 16.5 mm and up to 21.5 mm, the resonant frequency gradually decreases. For L_G values between 22.5 mm and 27.5 mm, the antenna resonates at approximately 6.672 GHz with a bandwidth of approximately 225 MHz.

In step 4, two additional identical rectangular slots (RECT3) were etched, as shown in Fig. 4, thereby transforming the patch into a three-step staircase configuration. The RECT3 slot dimensions were optimized by varying both length and width from 0.2 mm to 1.0 mm with a step size of 0.2 mm under a full ground-plane configuration. The corresponding parametric variation results, shown in Fig. 8(a), indicate that the resonant frequency remains nearly constant, with only slight variations in bandwidth. As in the previous steps, with the variations against ground plane length, the antenna resonates at frequencies above 10 GHz with a bandwidth of approximately 2.8 GHz, when L_G is varied from 5.5 mm to 16.5 mm. Beyond L_G =16.5 mm up to 21.5 mm resonant frequency decreases gradually and specifically, for L_G values between 22.5 mm and 27.5 mm, the antenna resonates around 6.68 GHz with a bandwidth of about 230 MHz. The parametric variation of L_G is shown in Fig. 8(b). The finalized geometrical parameters up to this step are summarized in Table II.

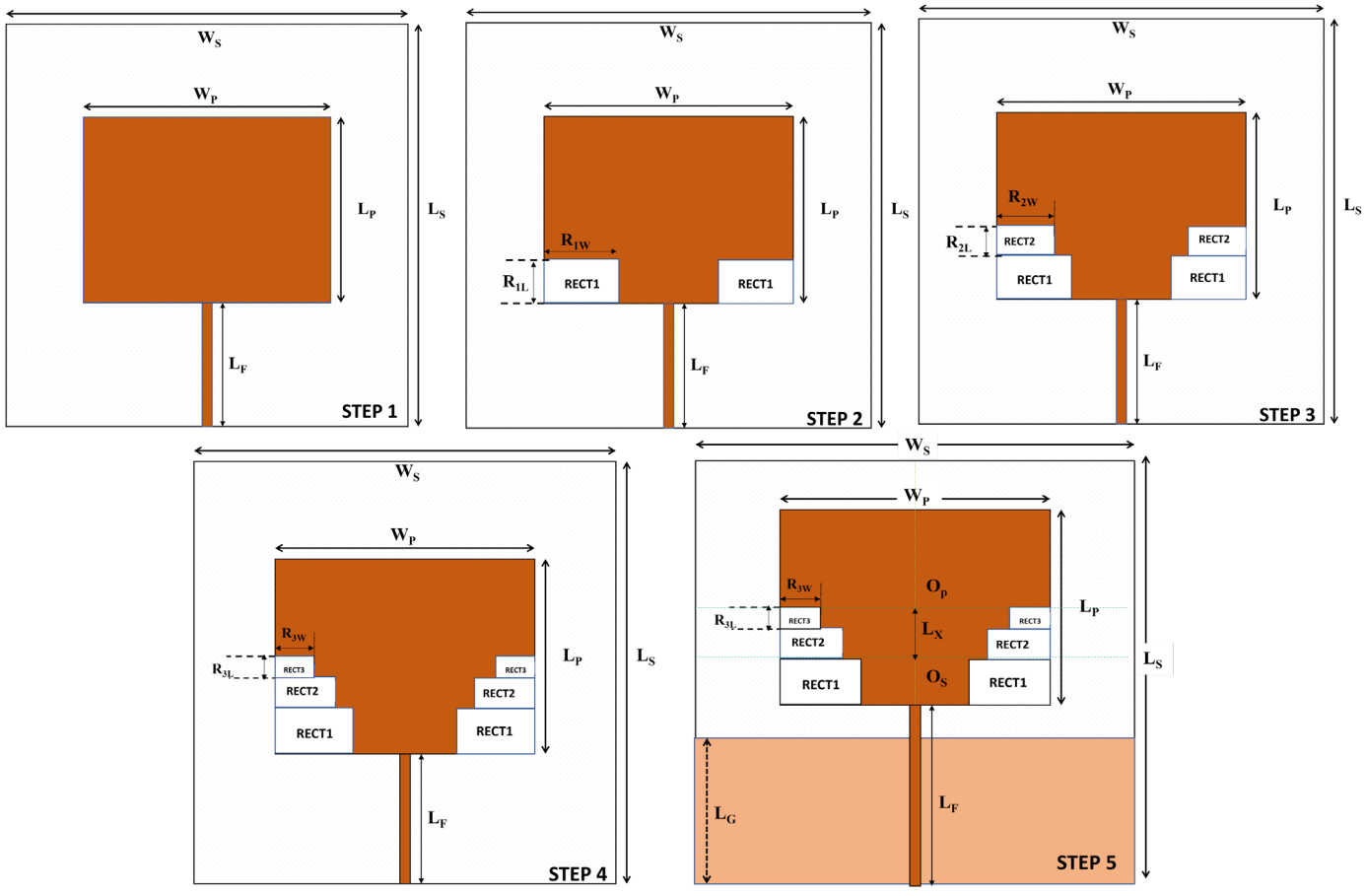


Fig. 4. Proposed antenna design steps.

TABLE II
PROPOSED ANTENNA DESIGN PARAMETER DIMENSIONS

Parameter	W_S	L_S	h	W_P	L_P	R_{1W}	R_{1L}	R_{2W}	R_{2L}	R_{3W}	R_{3L}
Dimension (mm)	27.5	27.5	1.6	16.86	12.5	2	1.6	1.4	1	0.8	0.4

The variation of L_G observed in the previous steps demonstrates that lower values of L_G yield significantly larger bandwidths compared to higher values, although these occur around 10 GHz. To shift this broader bandwidth into the Wi-Fi 6E band, the patch was displaced from its central position along the substrate length as depicted in Fig. 4 step 5. Here, points O_p and O_S represent the centers of the patch and the substrate's top surface, respectively. With this displacement, the feedline length (L_F) changes which impacts impedance matching and consequently the operating bandwidth. Accordingly, in step 5, a parametric analysis was conducted to examine the combined effects of ground plane length (L_G) and longitudinal displacement of the patch (L_X), relative to the substrate, on antenna performance. The L_G was varied from 5.5 mm to 27.5 mm with a step size of 1 mm, while the L_X was varied from 0 mm to 7.4 mm in steps of 0.2 mm. A total of 874, S_{11} responses were generated from the full parametric sweep, out of which only 32 combinations are presented in the analysis plot shown in Fig. 9, to ensure clarity and to effectively highlight the trends in impedance behavior with respect to variations in L_G and L_X. As evident from the results, for a fixed value of L_G, increasing L_X shifts the resonant frequency toward the Wi-Fi 6E band. In the previous design steps, the S_{11} response for L_G = 5.5 mm exhibits a resonance above 9.5 GHz. Following the introduction of patch displacement while keeping the L_G unchanged, the resonance shifts to approximately 7.73 GHz, 7.37 GHz, and 7.10 GHz for L_X values of 3.5 mm, 4.5 mm, and 5.5 mm, respectively. This indicates that increasing L_X effectively lowers the resonant frequency, thereby tuning the antenna toward the target Wi-Fi 6E band while preserving broader impedance bandwidth.

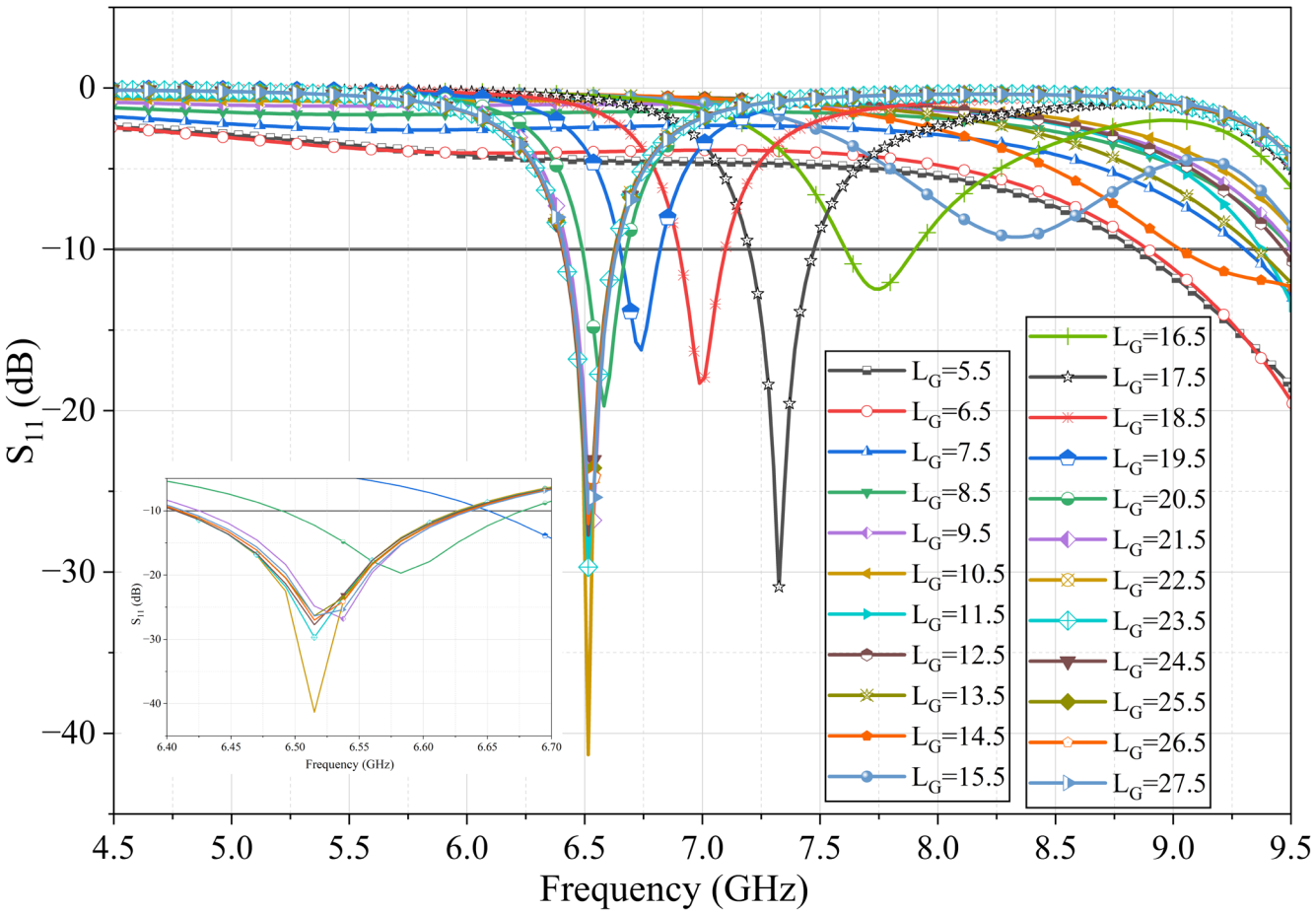
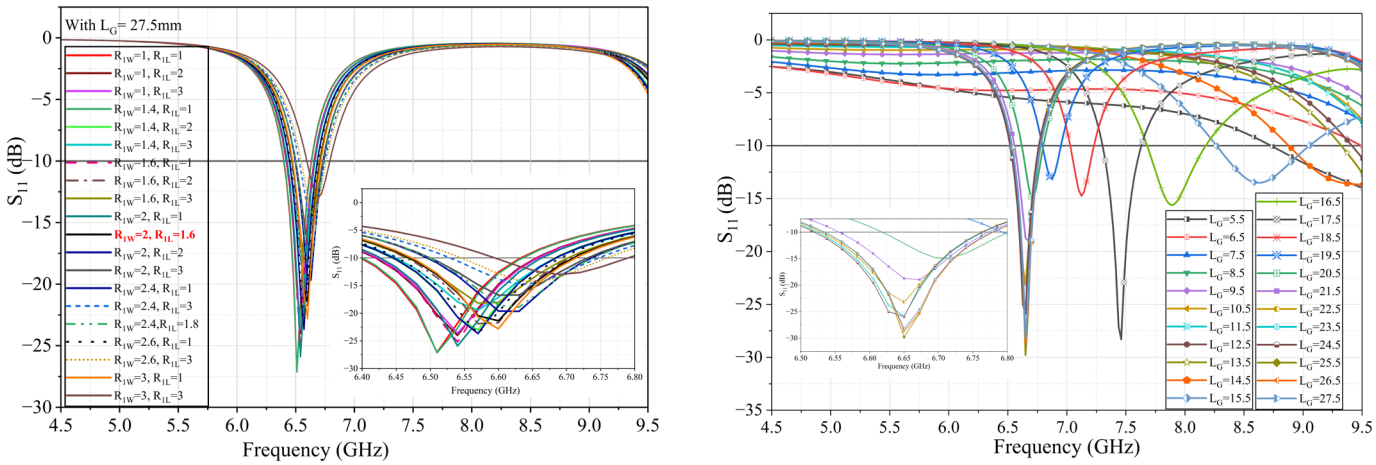


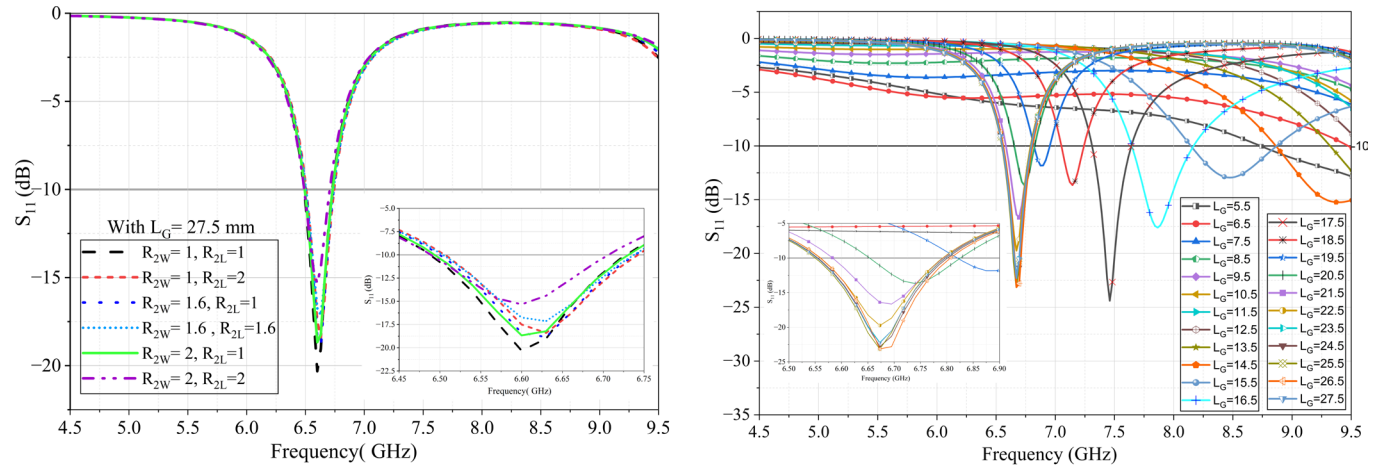
Fig. 5. Simulated S_{11} parametric analysis for design step 1 (Values of L_G are in mm).

Fig. 10 compares the simulated S_{11} vs frequency response of the antenna at each of the five design steps. For clarity, one representative curve from each parametric study (corresponding to Figs. 5, 6(b), 7(b), 8(b) and 9) is selected. As discussed earlier, reducing the L_G significantly enhances the impedance bandwidth but shifts the resonant frequency beyond the Wi-Fi 6E band. Therefore, for steps 1–4, the responses corresponding to the full L_G were selected, as they exhibit resonant frequencies closest to the target operating frequency. For design step 5, among all the parametric combinations investigated, the design with L_G = 8.5 mm and L_X = 4.5 mm was chosen as the representative response in Fig. 10. The comparison clearly demonstrates that the incorporation of slots slightly improved the bandwidth and final design step 5 successfully translates the broad impedance bandwidth into the Wi-Fi 6E frequency range while maintaining the wideband characteristics. The results obtained in step 5 were subsequently used to generate the dataset for performance optimization, as discussed in the following section.



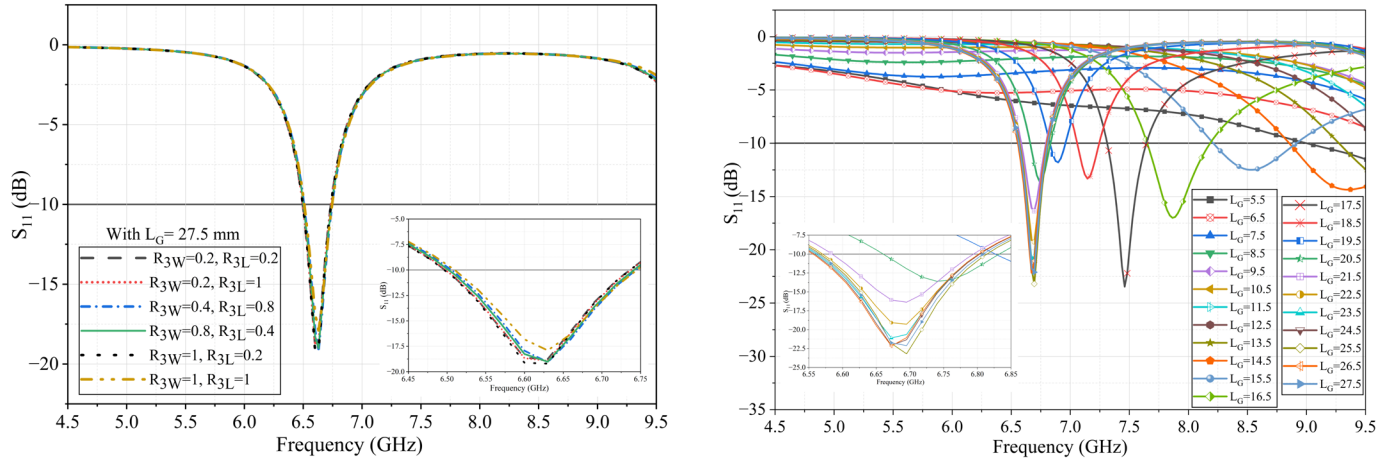
(a) (b)

Fig. 6. S_{11} parametric analysis for design step 2 **(a)** RECT1 slot dimension sweeps with full L_G **(b)** L_G tuning with finalized RECT1 dimensions (Values of R_{1W}, R_{1L} and L_G are in mm).



(a) (b)

Fig. 7. S_{11} parametric analysis for design step 3 **(a)** RECT2 slot dimension sweeps with full L_G **(b)** L_G tuning with finalized RECT2 dimensions (Values of R_{2W}, R_{2L} and L_G are in mm).



(a) (b)

Fig. 8. S_{11} parametric analysis for design step 4 **(a)** RECT3 slot dimension sweeps with full L_G **(b)** L_G tuning with finalized RECT3 dimensions (Values of R_{3W}, R_{3L} and L_G are in mm).

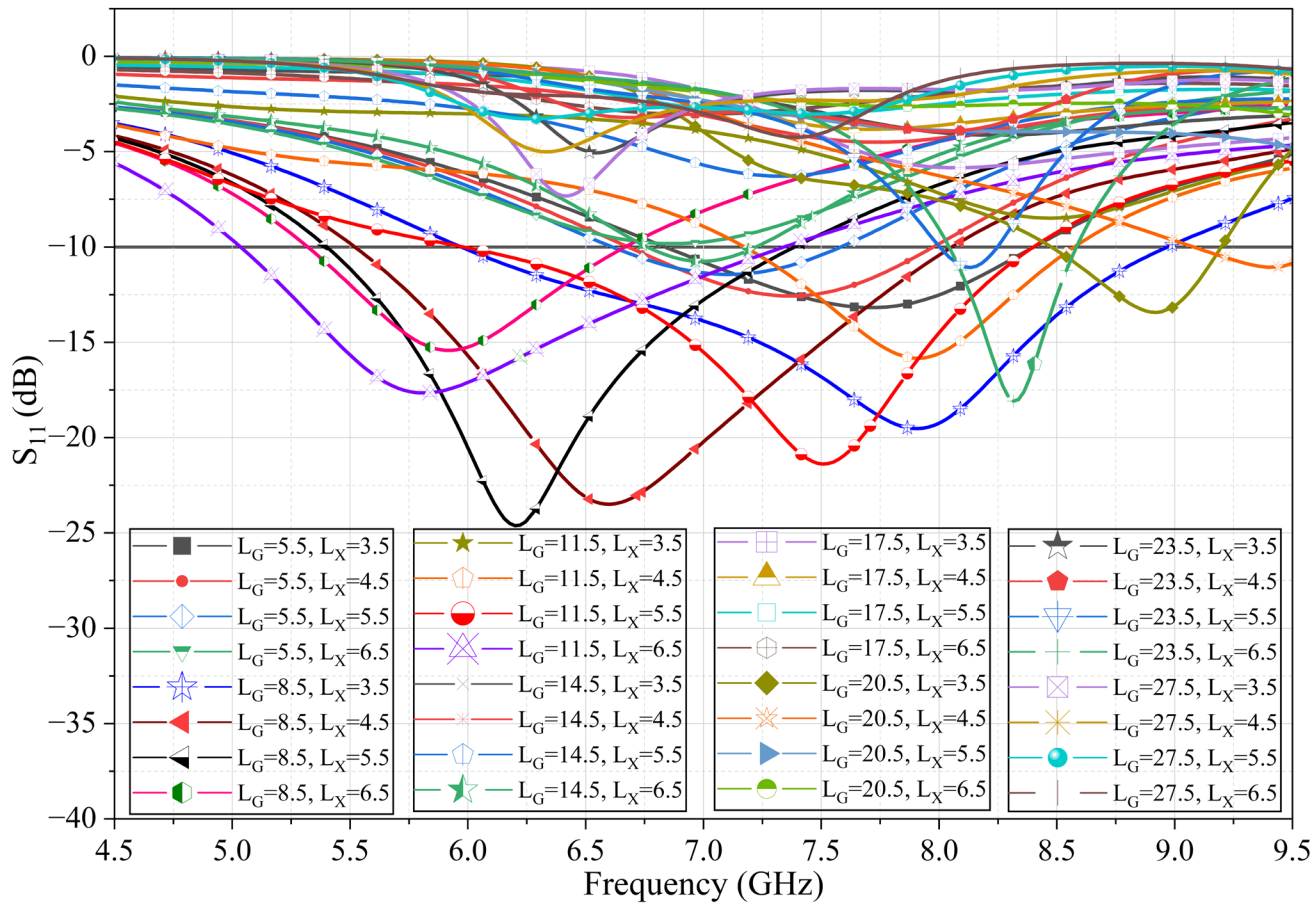


Fig. 9. S_{11} parametric analysis for design step 5 (Values of L_X and L_G are in mm).

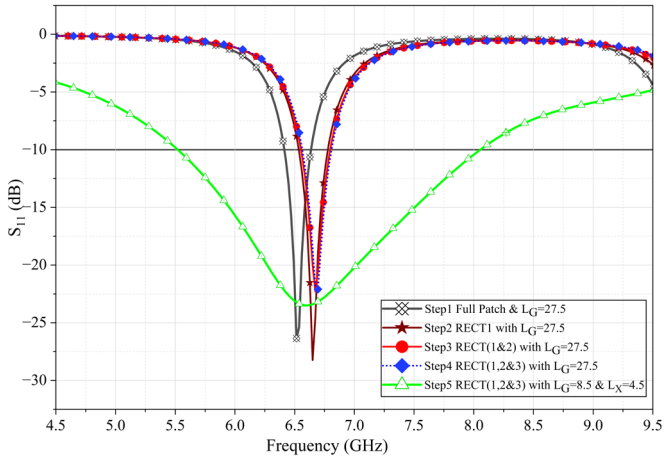


Fig. 10. Comparison of S_{11} vs frequency plot of all steps (1-5) (Values of L_X and L_G are in mm).

IV. Antenna Design Optimization

To ascertain the optimal value of longitudinal displacement of the patch on substrate surface (L_X) and ground plane length (L_G), an antenna optimization procedure is conducted employing curve fitting and PSO [29]. Fig. 11 shows the flowchart of optimization process.

A. Polynomial Generation using Curve Fitting

To ensure comprehensive coverage of the Wi-Fi 6E band with favorable impedance matching, simulations were performed by varying the parameters L_X and L_G. The antenna's S_{11} parameter was evaluated across the frequency range of 3 GHz –15 GHz, with L_G varied between 5.5 mm and 27.5 mm and L_X between 0 mm and 7.4 mm. From the generated HFSS simulation results a dataset comprising 81 samples was selected, out of which 15 were reserved for validation. To establish the relationship between the L_G, L_X and antenna's resonant frequency (f_r), which is different for every combination of L_G, and L_X, a fifth-degree polynomial model was developed using MATLAB's Curve Fitting Toolbox. The obtained fifth degree polynomial curve fit (2), is:

$$\begin{aligned} f_r = {} & -557.4243 - 25.2992\,L_G + 577.2977\,L_X + \\ & 33.6323\,L_G^2 - 93.2471\,L_G L_X - 138.7450\,L_X^2 - \\ & 7.1754\,L_G^3 + 17.6662\,L_G^2 L_X - 4.1250\,L_G L_X^2 + \\ & 28.3007\,L_X^3 + 0.4814\,L_G^4 - 0.6068\,L_G^3 L_X - \\ & 1.7708\,L_G^2 L_X^2 + 2.5982\,L_G L_X^3 - 3.7483\,L_X^4 - \\ & 0.0034\,L_G^5 - 0.0518\,L_G^4 L_X + 0.2083\,L_G^3 L_X^2 - \\ & 0.2054\,L_G^2 L_X^3 + 0.0190\,L_G L_X^4 + 0.1431\,L_X^5 \end{aligned} \tag{2}$$

where, L_G and L_X are in mm and f_r is in GHz. The fitted model is then applied into PSO algorithm to determine the optimal antenna dimensions at target resonant frequency.

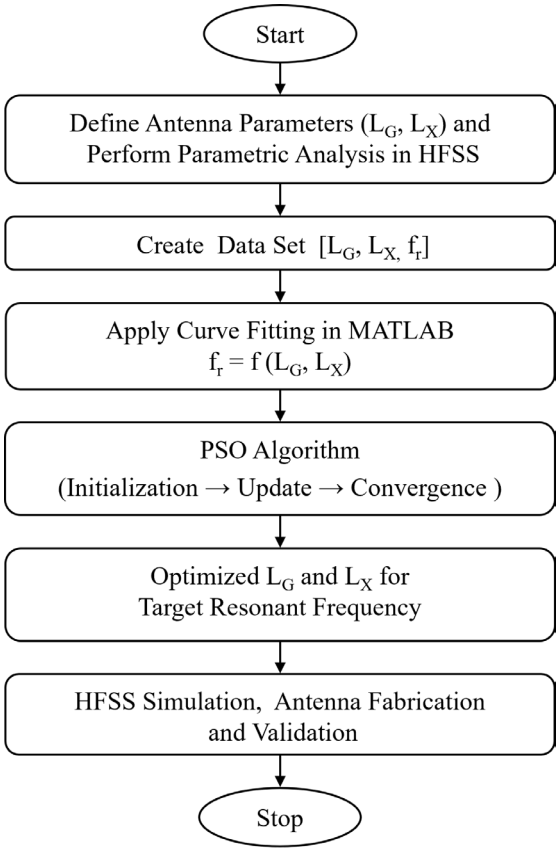


Fig. 11. Flowchart of optimization process.

B. Optimization using PSO

The PSO algorithm uses a population of particles (swarm) that iteratively explores the search space to find the optimal solution. Each particle represents a candidate solution in an N dimensional space and updates its velocity and position based on its personal best (p_{best}) and the global best (g_{best}) positions [24]. In this work, PSO is employed to optimize the parameters L_X and L_G for the target frequency of 6.525 GHz. The particle velocities and positions are updated according to (3), and (4), where v_i and x_i denote the velocity and position of the ith particle, n_1 and n_2 are random numbers, (w = 0.7) is the inertia weight, and k_1, k_2 are the cognitive and social acceleration coefficients. The algorithm terminates when the desired solution is achieved or the maximum number of iterations is reached [23], [24], [29].

$$v_i(t+1) = wv_i(t) + k_1 n_1[p_{best}(t) - x_i(t)] + k_2 n_2[g_{best}(t)\, x_i(t)] \quad (3)$$

$$x_i(t+1) = x_i(t) + v_i(t+1) \quad (4)$$

The polynomial (2), obtained from curve fitting is employed as a surrogate model to evaluate the fitness function within the PSO algorithm. Each particle in the swarm is characterized by a combination of the decision variables L_X and L_G, so that the position of a particle at any iteration is defined by specific values of L_X and L_G. The surrogate polynomial is evaluated at these coordinates to obtain the particle's fitness. The number of PSO iterations indicates how many times the swarm is updated and the g_{best} position is potentially improved.

The PSO algorithm employs the error function in (5) as the fitness function to optimize the design parameters L_X and L_G. The objective is to minimize the absolute deviation between the resonant frequency (f_r) and the target frequency of 6.525 GHz.

$$error = absolute\,(f_r - 6.525) \quad (5)$$

PSO is implemented in Python with a swarm of 25 particles and 100 iterations. The particle position corresponding to the global best provides the optimal values of L_X and L_G, obtained as 4.49 mm and 8.00 mm, respectively, yielding a minimal frequency error. The convergence behavior of the algorithm, in terms of error versus iteration number, is illustrated in Fig. 12.

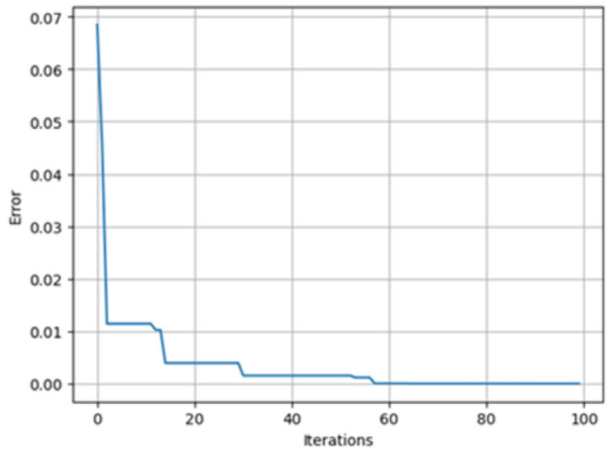
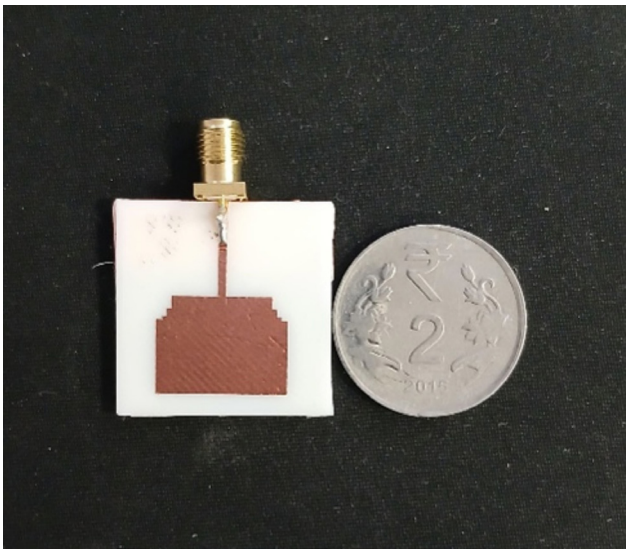


Fig. 12. Error vs number of iterations plot.

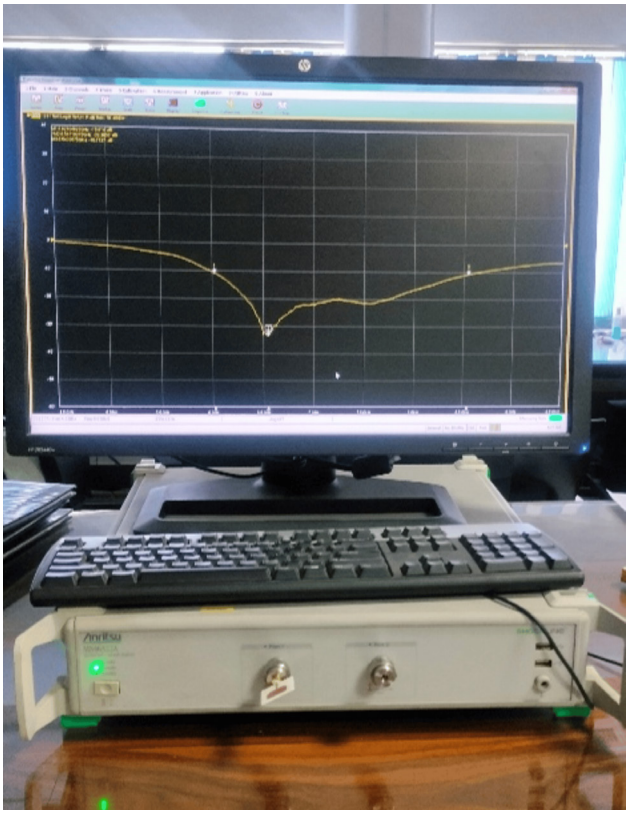
V. Results And Discussion

The proposed antenna was fabricated to validate the simulated performance, and the prototype is shown in Fig. 13(a). The S_{11} of the fabricated antenna was measured using a VNA, as illustrated in the measurement setup in Fig. 13(b). A quantitative comparison between simulated and measured results is summarized in Table III. Fig. 14 compares the simulated and measured S_{11} characteristics of proposed antenna. In simulation, the antenna provides a wide bandwidth from 5.58 to 7.69 GHz, corresponding to a fractional bandwidth of 38.26%. The measured results show bandwidth spanning 5.98 to 8.62 GHz, yielding a fractional bandwidth of 36.57%. The minor deviation between the simulated and measured results is mainly attributed to fabrication tolerances, such as substrate permittivity fluctuations during 3D printing of substrate, conductor thickness, and etching inaccuracies. Furthermore, connector and coaxial cable losses during measurement also contribute to the slight shift in the resonant frequency and impedance matching characteristics. Despite these variations, the measured results demonstrate robust impedance matching and sufficient bandwidth margin, thereby validating the antenna's suitability for practical Wi-Fi 6E applications. Fig. 15 illustrates the gain versus frequency

response of the proposed antenna, achieving a peak gain of 3.6 dBi within the Wi-Fi 6E operating band. The 2D radiation patterns in the x–z plane ($\phi = 0°$) and y–z plane ($\phi = 90°$) at 6.525 GHz are shown in Fig. 16. In the x–z plane, the antenna exhibits an approximately omnidirectional radiation pattern with a peak gain of 2.68 dBi, suitable for wide angular coverage. In contrast, the y–z plane presents a bidirectional (figure-eight) pattern achieving an absolute peak gain of 3.6 dBi along with deep, characteristic nulls at $\theta = \pm 90°$, illustrating the antenna's directional behavior in the principal planes.



(a)



(b)

Fig. 13. **(a)** Fabricated antenna **(b)** S_{11} measurement setup.

TABLE III
SIMULATION AND MEASUREMENT RESULTS

Parameters	f_r (GHz)	S_{11} (dB)	BW (GHz)	%BW
Simulation Results	6.44	-45.07	5.58 - 7.69	38.26
Measurement Results	6.50	-32.45	5.98 - 8.62	36.57

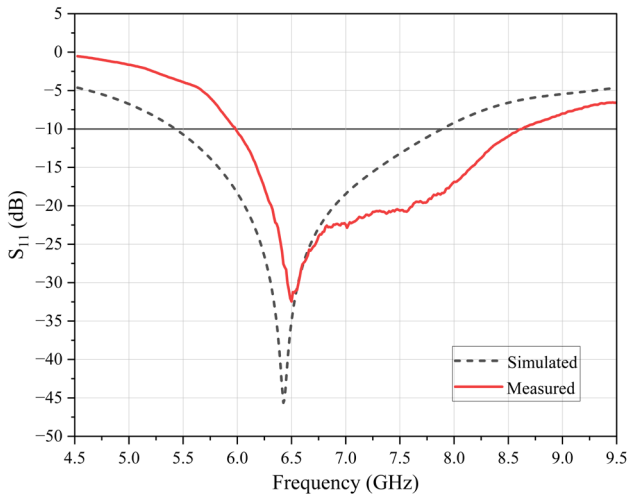


Fig. 14. Simulated and measured S_{11} plot

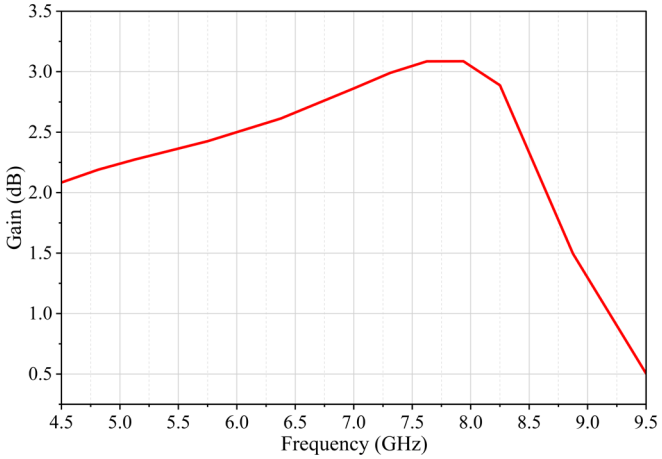


Fig. 15. Gain versus frequency plot of proposed antenna.

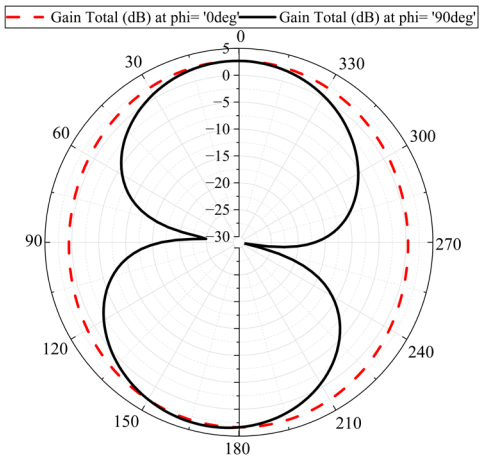


Fig. 16. Radiation pattern at 6.525 GHz.

Fig. 17 illustrates the surface current distribution at 6.525 GHz. Strong current concentration is observed along the feed line and feed–patch junction, indicating efficient energy transfer and excitation of the radiating patch.

Table IV compares the proposed antenna with other reported Wi-Fi 6/6E antennas employing different antenna configurations and substrate materials. It is evident that the proposed antenna fabricated on a 3D-printed ASA substrate achieves a measured −10 dB impedance bandwidth of 2.64 GHz (5.98–8.62 GHz) covering the complete Wi-Fi 6E band while maintaining a compact electrical size of $0.6\lambda_0 \times 0.6\lambda_0 \times 0.035\lambda_0$. Although some reported antennas [2]-[4], [6], and [7] achieve comparable bandwidth or higher gain, they rely on structurally complex solutions such as MIMO configurations [3], [7], array structures [6], air-cavity-based designs [4], and metal-backed cavity structures [5], which increase fabrication complexity and cost. Moreover, antennas reported in [1], [4]-[7], and [17] exhibit larger electrical dimensions than the proposed design. The proposed antenna is specifically optimized to provide complete coverage of the Wi-Fi 6E band, while maintaining a compact size, simple geometry, and good radiation performance. Therefore, it offers a practical trade-off among bandwidth, compactness, gain, and ease of fabrication for Wi-Fi 6E applications.

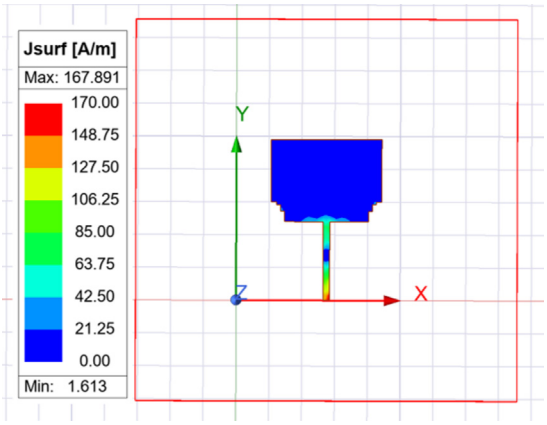


Fig. 17. Surface current distribution of proposed antenna at 6.525 GHz.

TABLE IV
COMPARATIVE STUDY OF PROPOSED ANTENNA WITH EXISTING DESIGNS

Year	Ref. No.	Antenna type/structure	Antenna dimensions ()	Substrate material	S_{11} (dB)	Operational frequency range (GHz)	BANDWIDTH (MHz)	Gain (dB)	OPTIMIZATION APPROACH
2021	[2]	Planar Antenna	0.94 × 0.065 × 0.009	FR4	-29	2.40-2.48/ 5.150-7.125	82/1975	2.84dBi	None
2021	[3]	MIMO antenna	0.87 × 0.65 × 0.014	Rogers RT6010	-13.5	3.45-3.65/ 5.92-10.83	200/4910	Not reported	None
2022	[1]	Asymmetric bow-tie antenna	1.96 × 1.96 × 0.035	FR4	-15	2.22-2.81 / 5.08-7.79	590/2710	Not reported	None
2022	[5]	Dual Half-Open Cavity Antenna (HOCA) Pair	0.22 × 0.26 × 1.31	Metal cavity structure	- 22.67	5.15-5.82 / 5.925-7.125	675/1200	5dBi	None
2023	[4]	Stacked embedded DPA	1.22 × 0.96 × 1.42	FR4_epoxy	- 25	4.63-7.58	2950	8.47dBic	None
2024	[17]	Patch antenna	0.7 × 0.6 × 0.035	3D printed ASA	≤ -12	5.17-9.34	4170	3.45dBi	None
2025	[6]	Slotted MPA 2 ×2 array	≥ 1.32 × 1.45 × 0.07	F4B	≤ -20	5.10-7.20	2100	14.1 dBi	None
2026	[7]	4-Port DGS-MIMO Antenna	1.63 × 1.63 × 0.017	FR4	≤ -10	5.10-7.20	2100	Not reported	None
This Work	--	Proposed antenna	0.6 × 0.6 × 0.035	3D printed ASA	- 32.45	5.98-8.62	2640	3.6 dBi	Curve fitting and PSO

Note: All electrical dimensions are expressed in terms of free space wavelength λ_0 at 6.525 GHz

VI. CONCLUSION

This work presents compact 3D-printed ASA-substrate wideband antenna for Wi-Fi 6E applications, optimized using a hybrid curve-fitting and PSO-based methodology. To the best of the authors' knowledge, this is the first integration of curve fitting and PSO-driven optimization in a 3D-printed ASA antenna framework for Wi-Fi 6E band operation. The antenna achieves a measured operating bandwidth from 5.98–8.62 GHz, covering the Wi-Fi 6E band enabling its use in terrestrial wireless applications. The selected 3D-printed ASA substrate offers resistance to weathering, UV exposure, and chemical effects, making the antenna suitable for outdoor deployments such as smart city infrastructure, outdoor Wi-Fi access points, and IoT gateway nodes. The close agreement between simulated and measured results validates the effectiveness of the proposed design and optimization methodology, indicating the suitability of the antenna for practical wideband wireless systems.

References

[1] C.-C. Ku, M.-T. Wu, and M.-L. Chuang, "Multiband antenna design for Wi-Fi 6E applications," in *Proc. IEEE Int. Conf. Consumer Electronics*, Taipei, Taiwan, 2022, pp. 383–384, DOI: 10.1109/ICCE-Taiwan55306.2022.9869129.

[2] W.-C. Jhang and J.-S. Sun, "Small antenna design of triple band for Wi-Fi 6E and WLAN applications in the narrow border laptop computer," *Int. J. Antennas Propag.*, 2021, Art. 7334206, pp. 1–8, DOI: 10.1155/2021/7334206.

[3] H. E. O. E. Bakali, A. Zakriti, A. Farkhsi, A. Dkiouak, and M. El Ouahabi, "Design and realization of dual-band notch UWB MIMO antenna in 5G and Wi-Fi 6E using hybrid technique," *Prog. Electromagn. Res. C*, vol. 116, 2021, pp. 1–12, DOI: 10.2528/PIERC21080701.

[4] H. Jiang, N. Yan, K. Ma, and Y. Wang, "A wideband circularly polarized dielectric patch antenna with a modified air cavity for Wi-Fi 6 and Wi-Fi 6E applications," *IEEE Antennas Wireless Propag. Lett.*, vol. 22, no. 1, pp. 213–217, 2023, DOI: 10.1109/LAWP.2022.3201077.

[5] X. Zhang, L. Sun, Y. Li, and Z. Zhang, "A broadband dual-antenna pair based on half-open cavity with horizontally polarized radiation for Wi-Fi 6/6E applications," *IEEE Trans. Antennas Propag.*, vol. 70, no. 6, pp. 4250–4258, 2022, DOI: 10.1109/TAP.2022.3140322.

[6] Z. Zhu, S. Gao, and L. Chang, "Low-profile wideband slotted microstrip patch antenna array based on higher-order mode for Wi-Fi 6/6E application," in *Proc. 4th Int. Conf. Electronic Information and Communication Engineering (EICE)*, Guangzhou, China, 2025, Art. 012022, DOI: 10.1088/1742-6596/2991/1/012022.

[7] M. A. Begum, T. Yuvaraj, and R. Krishnamoorthy, "Design and analysis of a DGS-MIMO antenna for Wi-Fi 5/6/6E applications," *Telecommun. Syst.*, vol. 89, p. 76, 2026, DOI: 10.1007/s11235-026-01456-6.

[8] P. Rani, B. S. Dhaliwal, and A. Kumar, "Analysis of 3-D printed meta-structure substrates for microstrip patch antenna design," *Discover Sensors*, vol. 1, Art. 30, 2025, DOI: 10.1007/s44397-025-00031-z.

[9] R. Cicchetti, E. Miozzi, and O. Testa, "Wideband and UWB antennas for wireless applications: A comprehensive review," *Int. J. Antennas Propag.*, vol. 2017, Art. 2390808, pp. 1–45, 2017, DOI: 10.1155/2017/2390808.

[10] T. Tewary, S. Maity, S. Mukherjee, A. Roy, P. P. Sarkar, and S. Bhunia, "High gain miniaturized super-wideband microstrip patch antenna," *Int. J. Commun. Syst.*, vol. 35, no. 11, pp. 1–24, 2022, DOI: 10.1002/dac.5181.

[11] A. K. Vallappil, B. A. Khawaja, M. K. A. Rahim, M. N. Iqbal, H. T. Chattha, and M. F. B. M. Ali, "A compact triple-band UWB inverted triangular antenna with dual-notch band characteristics using SSRR metamaterial structure," *Fractal Fract.*, vol. 6, no. 8, Art. 422, 2022, DOI: 10.3390/fractalfract6080422.

[12] S. S. Carvalho, J. R. V. Reis, A. Mateus, and R. F. S. Caldeirinha, "Exploring design approaches for 3-D printed antennas," *IEEE Access*, vol. 12, pp. 10718–10735, 2024, DOI: 10.1109/ACCESS.2024.3354372.

[13] S. Moscato, R. Bhar, T. Le, M. Pasian, M. Bozzi, L. Perregrini, and M. M. Tentzeris, "Infill-dependent 3-D printed material based on NinjaFlex filament for antenna applications," *IEEE Antennas Wireless Propag. Lett.*, vol. 15, pp. 1506–1509, 2016, DOI: 10.1109/LAWP.2016.2516101.

[14] D. Kalaš, K. Šíma, P. Kadlec, R. Polanský, R. Soukup, J. Řeboun, and A. Hamáček, "FFF 3D printing in electronic applications: Dielectric and thermal properties of selected polymers," *Polymers*, vol. 13, no. 21, Art. 3702, 2021, DOI: 10.3390/polym13213702.

[15] A. M. Kulkarni, G. Saini, and S. S. Pattnaik, "Design of miniaturized antenna array on 3-D printed PLA substrate with fractal ground," in *Proc. Microwaves, Antennas and Propagation Conf.*, Ahmedabad, India, 2023, pp. 1–5, DOI: 10.1109/MAPCON58678.2023.10463825.

[16] C. Jain, B. S. Dhaliwal, and R. Singh, "On 3-D printed acrylonitrile butadiene styrene-based sensors," *J. Mater. Eng. Perform.*, vol. 31, no. 11, pp. 8760–8774, 2022, DOI: 10.1007/s11665-022-06884-4.

[17] Manju, G. Saini, and B. S. Dhaliwal, "Design and analysis of a 3-D printed ASA substrate based antenna for Wi-Fi 6E application," in *Proc. Int. Conf. Electrical, Electronics and Computing Technologies*, Noida, India, 2024, pp. 1–5, DOI: 10.1109/ICEECT61758.2024.10738921.

[18] Ç. Bolat, F. Demircan, İ. Gür, B. Yalçın, R. Şener, and A. Ercetin, "Hardness and Surface Roughness of 3D-Printed ASA Components Subjected to Acetone Vapor Treatment and Different Production Variables: A Multi-Estimation Work via Machine Learning and Deep Learning," *Polymers*, vol. 17, no. 21, Art. 2881, 2025, DOI: 10.3390/polym17212881.

[19] N. Vidakis, M. Petousis, N. Michailidis, D. Sagris, C. David, V. Papadakis, M. Spyridaki, A. Argyros, I. Valsamos, E. Dimitriou, and E. Kymakis, "Thermomechanical recyclability of acrylonitrile styrene acrylate (ASA) for cyclic economy-driven MEX additive manufacturing," *Cleaner Engineering and Technology*, vol. 25, Art. 100925, 2025, DOI: 10.1016/j.clet.2025.100925.

[20] A. Z. Hameed, S. Aravind Raj, J. Kandasamy, M. A. Shahzad, and M. A. Baghdadi, "3D printing parameter optimization using Taguchi approach to examine acrylonitrile styrene acrylate (ASA) mechanical properties," *Polymers*, vol. 14, no. 16, Art. 3256, 2022, DOI: 10.3390/polym14163256.

[21] A. Y. I. Ashyap, Z. Z. Abidin, S. H. Dahlan, H. A. Majid, S. M. Shah, M. R. Kamarudin, and A. Alomainy, "Compact and low-profile textile EBG-based antenna for wearable medical applications," *IEEE Antennas Wireless Propag. Lett.*, vol. 16, pp. 2550–2553, 2017, DOI: 10.1109/LAWP.2017.2732355.

[22] D. Jang, J.-Y. Lee, and H. Choo, "Design of a stacked dual-patch antenna with 3-D printed thick quasi-air substrates and a cavity wall for wideband applications," *Appl. Sci.*, vol. 14, no. 4, Art. 1571, 2024, DOI: 10.3390/app14041571.

[23] R. Verma and D. Srivastava, "Design, optimization and comparative analysis of T-shape slot loaded microstrip patch antenna using PSO," *Photon. Netw. Commun.*, vol. 38, pp. 1–13, 2019, DOI: 10.1007/s11107-019-00867-7.

[24] B. S. Dhaliwal and S. S. Pattnaik, "Development of PSO–ANN ensemble hybrid algorithm and its application in compact crown circular fractal patch antenna design," *Wireless Pers. Commun.*, vol. 96, pp. 135–152, 2017, DOI: 10.1007/s11277-017-4157-8.

[25] B. S. Dhaliwal, A. Kaur, S. Pattnaik, and S. S. Pattnaik, "Optimization of hybrid fractal antenna using curve fitting and GA approach for RF energy harvesting application," in *Proc. IEEE Indian Conf. Antennas and Propagation*, Ahmedabad, India, 2019, pp. 1–4, DOI: 10.1109/InCAP47789.2019.9134573.

[26] G. Zou, H. Gronqvist, J. P. Starski, and J. Liu, "Characterization of liquid crystal polymer for high frequency system-in-a-package applications," *IEEE Trans. Adv. Packag.*, vol. 25, no. 4, pp. 503–508, 2002, DOI: 10.1109/TADVP.2002.807593.

[27] C. A. Balanis, *Antenna Theory: Analysis and Design*, 3rd ed. New Delhi, India: Wiley India Pvt. Ltd., 2013, p. 528.

[28] J.-M. Heinola and K. Tolsa, "Dielectric characterization of printed wiring board materials using ring resonator techniques: a comparison of calculation models," *IEEE Trans. Dielectr. Electr. Insul.*, vol. 13, no. 4, pp. 717–726, 2006, DOI: 10.1109/TDEI.2006.1667729.

[29] A. M. Kulkarni, G. Saini, S. S. Pattnaik, and S. Pattnaik, "Antenna array fault diagnosis using particle swarm optimized CNN," in *Proc. Microwaves, Antennas and Propagation Conf.*, Ahmedabad, India, 2023, pp. 1–6, DOI: 10.1109/MAPCON58678.2023.10464080.